Journal of Magnetism and Magnetic Materials 380 (2015) 353–359

Contents lists available at ScienceDirect

Journal of Magnetism and Magnetic Materials

journal homepage: www.elsevier.com/locate/jmmm

# Heat transition during magnetic heating treatment: Study with tissue models and simulation

Franziska Henrich [a,b], Helene Rahn [a,*], Stefan Odenbach [a]

[a] Technische Universität Dresden, Institute of Fluid Mechanics, Chair of Magnetofluiddynamics, 01062 Dresden, Germany
[b] Max Planck Institute for Polymer Research, Physics at Interfaces, 55128 Mainz, Germany

ARTICLE INFO

*Article history:*
Received 30 June 2014
Received in revised form
30 August 2014
Accepted 2 September 2014
Available online 10 September 2014

*Keywords:*
Heat transfer
Magnetic heating
Phantom
Simulation

ABSTRACT

The magnetic heating treatment (MHT) is well known as a promising therapy for cancer diseases. Depending on concentration and specific heating power of the magnetic material as well as on parameters of the magnetic field, temperatures between 43 and 55 °C can be reached. This paper deals with the evaluation of heat distribution around such a heat source in a tissue model, thereby focusing on the heat transfer from tissue enriched with magnetic nanoparticles to regions of no or little enrichment of magnetic nanoparticles.

We examined the temperature distribution with several tissue phantoms made of polyurethane (PUR) with similar thermal conductivity coefficient as biological tissue. These phantoms are composed of a cylinder with one sphere embedded, enriched with magnetic fluid. Thereby the spheres have different diameters in order to study the influence of the surface-to-volume ratio.

The phantoms were exposed to an alternating magnetic field. The magnetically induced heat increase within the phantoms was measured with thermocouples. Those were placed at defined positions inside the phantoms. Based on the measured results a 3-dimensional simulation of each phantom was built.

We achieved an agreement between the measured and simulated temperatures for all phantoms produced in this experimental study. The established experiment theoretically allows a prediction of temperature profiles in tumors and the surrounding tissue for the potential cancer treatment and therefore an optimization of e.g. the respective magnetic nanoparticles concentrations for the desirable rise of temperature.



## 1. Introduction

Since the introduction of magnetic carriers to the field of biomedical application, the research activities are increasing continuously but especially in cancer treatment [1–22]. Just to name two of magnetically assisted cancer treatments—these are magnetic drug targeting (MDT) [5–8], and the magnetic heating treatment (MHT) [9–11], which is also known as magnetic hyperthermia [12] or magnetic fluid hyperthermia [13–17].

MDT is a magnetically guided and controlled drug delivery into the tumoral region. The magnetic nanoparticles act as drug carriers. Thereby the focus is on enabling a high but local concentration of the chemotherapeutic agent within the target region. Consequently, there is a high accumulation of the chemotherapeutic agent within the tumor and no or minor enrichment of the drug in other parts of the patient's body [18,19].

Magnetic heating treatment is also a promising local and minimal-invasive cancer treatment with no or minor negative side effects. Already in 1957 Gilchrist suggested magnetic particles for local temperature increase in a target region induced by an external magnetic field [23]. Since then, scientific investigation of magnetically induced heat generation continues as presented in [18].

MHT is also based on magnetic nanoparticles but the working principle is characterized through a different mechanism. In this case the magnetic nanoparticles are used to induce heat locally by an external alternating magnetic field. The magnetic nanoparticles are guided or directly injected to the target region. Subsequently the target region is exposed to an alternating magnetic field. As consequence temperatures of up to 71 °C [10] within the respective biological tissue (e.g. the tumor) can be established, due to the remagnetisation processes which occur in magnetic nanoparticles. If the generated temperatures are between 42 °C and 45 °C and the treatment duration is 30 min to 60 min the procedure is defined as hyperthermia [9,10]. Magnetically assisted thermoablation is defined if the maximum temperatures are above 50 °C and the duration is a few minutes only. Successful documentation of thermoablation applied to laboratory animals are presented in [11]. Here temperature

* Corresponding author.
*E-mail address:* helene.rahn@tu-dresden.de (H. Rahn).

http://dx.doi.org/10.1016/j.jmmm.2014.09.006
0304-8853/

rises of $\Delta T = 13$ K to 34 K have been detected during the treatment. The subsequent analysis of the respective tissue showed local damage under the applied conditions [11].

In this particular research we are focusing on magnetically induced heat generation as used for MHT. Our primary target is the prediction of temperature profiles in a tumor and its surrounding tissue during MHT.

Among other things one of the crucial parameters for the efficiency of magnetically assisted heating treatment is the distribution of the magnetic material within the respective tissue. This means that the magnetic nanoparticles have to be spread homogeneously within the respective tissue and existing in a sufficient quantity. These factors strongly influence the heat generation and thus the possible temperature increase. In case of an insufficient enrichment within the tumoral tissue the heat transfer to the non-enriched regions of the tumor shall be sufficient enough to affect the surrounding tumor tissue.

This can be regarded as the motivation for our experimental approach—understanding the heat transfer process between tissue which is enriched with magnetic nanoparticles and tissue which is not. We have performed the heat transfer study with geometrically simple phantoms composed of a tissue substitute and magnetic nanoparticles. The experimental results provided the basics for a simulation model. The simulation enabled a determination of temperature profiles inside a tumor based on its surrounding tissue during MHT.

Andrä et al. [24] already examined heat transfer phenomena in biological tissue caused by magnetic particles in the micrometer range. Furthermore, the temperature measurements in tumor or animal models are commonly performed with thermocouples which are placed inside the respective tissue. The piercing of the tumoral tissue can lead to formation of metastasis [25]. Thus we have decided to focus on a phantom with simple geometry and predictable behavior of the tissue substitute to understand the heat transfer phenomena. As a consequence, an external temperature measurement together with the established simulation model shall enable the determination of the temperature inside the tumor during magnetic heating.

We present four cylindrical phantoms (A, B, C, D) made of an elastomer with similar heat conduction behavior as biological tissue. In contrast to [26,27], the phantoms include one or two embedded spheres. These spheres consist of elastomer enriched with magnetic nanoparticles. The spherical shape enriched with magnetic nanoparticles where chosen due to the lower surface to volume ratio with equal volume in order to reduce the heat losses in the enriched areas.

The phantoms were installed into an experimental set up. Then, the phantoms were exposed to an alternating magnetic field according to a protocol of MHT [10]. The used alternating magnetic field was in contrast to [26,27] biocompatible (see Section 2.2). The temperature increase was measured with thermocouples.

The obtained results were used to implement a simulation procedure enabling a determination of the temperatures inside tissue during magnetic heating.

## 2. Experimental setup

### 2.1. Measuring methods and components

In the following section we briefly describe the measuring methods and the components used for the phantom production.

#### 2.1.1. Temperature measurement

The temperature in the phantoms was measured with thermocouples type T. The thermocouple wires have a diameter of 0.08 mm and consist of copper and constantan [28]. The amount of nickel is negligible so the self-heating induced by the alternating magnetic field is very small. For the magnetic heating experiment five thermocouples have been inserted into each phantom.

#### 2.1.2. Magnetic examination

The amount of magnetic particle inside the magnetic fluid as well as of the material the phantoms were built of was verified by vibrating sample magnetometer (VSM) measurements utilizing a 7407 from Lake Shore Cryoteronics, Inc [29].

#### 2.1.3. X-ray microcomputed tomography examination (XμCT)

The exact positions of the thermocouples inside of the phantoms were detected using X-ray-tomography. For these 3-dimensional measurements a XμCT equipment named "TomoTU" located at the chair of Magnetofluiddynamics, Measuring and Automation Technology at TU Dresden, Germany [30,31] was used.

The digital tomographic data provided the exact positions of the thermocouples inside the phantoms for the latter simulation.

#### 2.1.4. Tissue substitute material

The tissue models consist of the polyurethane (PUR) Bectron® PU 4526 manufactured by Elantas Beck. As described in [26] this PUR has similar heat transfer properties as human tissue. The heat conductivity in human tissue is depending on the blood flow. Tumor tissue is well perfused and has a heat conductivity of $\lambda = 0.641$ W/(m K) [32]. The used PUR PU 4526 has a heat conductivity of 0.64 W/(m K) [33].

#### 2.1.5. Magnetic fluid

As biocompatible ferrofluids are water based and water mixed with polyurethane leads to a production of foam, the commercial ferrofluid APG 513A [34] was used. The magnetic particles consist of magnetite, which is also used in biocompatible ferrofluids [35]. The particles with a diameter of 10 nm of the ferrofluid APG 513A are suspended in synthetic ester, which cannot be regarded as biocompatible. The mean particle diameter as well as nanoparticles concentration of 7.2 mg/ml [4] have also been checked with a VSM measurement.

With the combination of the polyurethane PU 4526 and the ferrofluid APG 513A a long-term stable, homogeneous material is build.

### 2.2. Magnetic field

For the magnetic heating an alternating magnetic field is necessary. The alternating magnetic field was generated by using an inductive coil. The coil has 22 windings, an inner diameter of 27 mm. The frequency $f$ is $284 \pm 0.1$ kHz and the magnetic field strength $H$ can vary between 4.4 kA/m and 8.7 kA/m. Because the product of $H \times f \leq 5 \times 10^9$ A/(m s), the alternating magnetic field is in a range that is usually assumed to be biocompatible [36].

### 2.3. Tissue model

Four different cylindrical tissue models were produced (phantom A, B, C, D). Phantoms A, B, C contain one spherical area of PUR enriched with ferrofluid. Thereby the concentration of magnetite in the elastomer was about 9.36 mg/ml and 12.38 mg/ml. The results of magnetic measurements are shown in Table 1. These spheres stand for the enriched tumor tissue.

The diameter of the spheres within the three phantoms is different in order to vary the surface to volume ratio (Table 2). These areas are surrounded by a pure PUR cylindrical area (diameter 18 mm) to model the surrounded non-enriched material.

Phantom D has also a cylindrical body (diameter 18 mm) featuring two ferrofluid enriched spheres (diameter 10 mm) which are embedded. With this phantom it is possible to simulate the

temperature profile between two nanoparticle enriched regions. Fig. 1 show a technical drawing of the phantoms A to D and the positions of the thermocouples inside the phantoms.

For the temperature measurement thermocouples were inserted into the phantoms. Their exact position positions have been verified with XμCT. The evaluation of the 3-dimensional tomographic data provides the thermocouple positions with an accuracy in the micrometer range.

Fig. 2(a) shows an axial slice of radiographic grey scale image of the phantom A. One can clearly see the thermocouples' heads and wires. Fig. 3(b) images a slice along the red line in Fig. 3(a). The digital tomographic data has been analyzed with respect to positions of the thermocouples heads. These exact positions have been used for the simulation.

### 2.4. Experimental implementation

A schematic sketch of the experimental setup is shown in Fig. 3.

**Table 1**
Magnetic particle concentration in phantoms A, B, C, D.

| Phantom | Concentration [$mg_{magnetite}/ml_{PUR}$] |
|---|---|
| A | $12.38 \pm 0.6$ |
| B | $10.65 \pm 0.6$ |
| C | $12.38 \pm 0.6$ |
| D1 | $9.36 \pm 0.6$ |
| D2 | $11.35 \pm 0.6$ |

**Table 2**
Diameter of the spheres enriched with ferrofluid and the surface to volume ratio of the different phantoms.

| Phantom | Diameter [mm] | Surface-to-volume ratio |
|---|---|---|
| A | 5 | 0.6 |
| B | 10 | 0.3 |
| C | 15 | 0.2 |
| D | 10 | – |

The phantoms were placed in a water bath with a constant temperature of 37 °C to guarantee similar surrounding condition as in human bodies. During the experiments the water bath with a phantom inside was placed in the center of the coil (as shown in Fig. 4). The thermocouples detect the temperature changes within the phantom. These changes are measured by a multimeter.

The measuring cycles were performed as described subsequently: after an initial temperature of 310.15 K inside the phantom was reached, the temperature has been measured for another five minutes. Then an alternating magnetic field applied to the tempered phantom. The magnetic heating was performed for 10 min. In this period of time, a saturation of the temperature has been observed. The temperature decrease has been detected for another 5 min after switching of the magnetic field.

### 2.5. Simulation

As mentioned in Section 1, the experimental results of the heat transfer were used for a simulation model. Thereby we used the finite element analysis software COMSOL Multiphysics [37].

The geometry was constructed following the design of the actual experimentally investigated phantoms. For phantoms A, B, and C the model consists of one sphere and for phantom D two spheres representing the ferrofluid enriched zone and a surrounding cylinder representing the PUR. The tempering of the phantoms induced through the water bath is made of another cylinder with a diameter of 20 mm and physical properties of water. A defined temperature of 310.15 K has been adjusted at the outer region of the cylinder simulating the water bath. The temperature rise generated by re-magnetization processes is implemented into the simulation as a heat source inside the spheres. To simulate the increasing of the temperature due to the magnetic heating, a heat source in the center of the simulated sphere was implemented. For each magnetic field strength one heating capacity was calculated with the following equation $\dot{q} = c_p \times \Delta T \times \rho \times k$ with $c_p = 1400$ J/(kg K); $\rho = 1546$ kg/m$^3$ matching coefficient $k = 28.8$ s$^{-1}$ and $\Delta T$ temperature difference which is based on the measurement. Table 3 shows the used heating capacities.

For the simulation we have adjusted the phantoms' diameter to 19 mm and its height to 40 mm. The real diameters and heights of the phantoms vary slightly due to the production process. The diameters of the spheres have been assumed to 5 mm, 10 mm, and

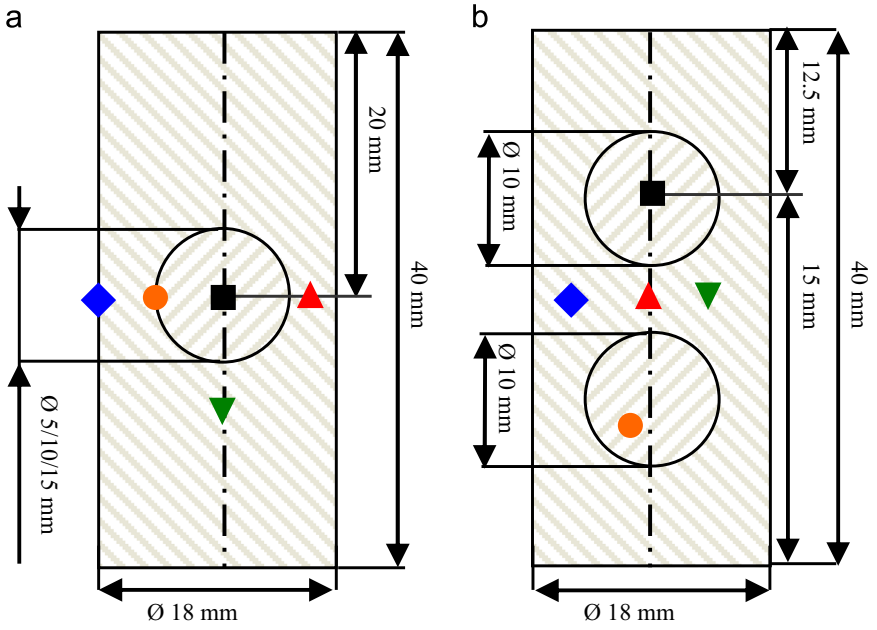


**Fig. 1.** Technical drawing: (a) of the phantoms A–C and (b) of the phantom D; with schematic positions of thermocouples inside the Phantoms.

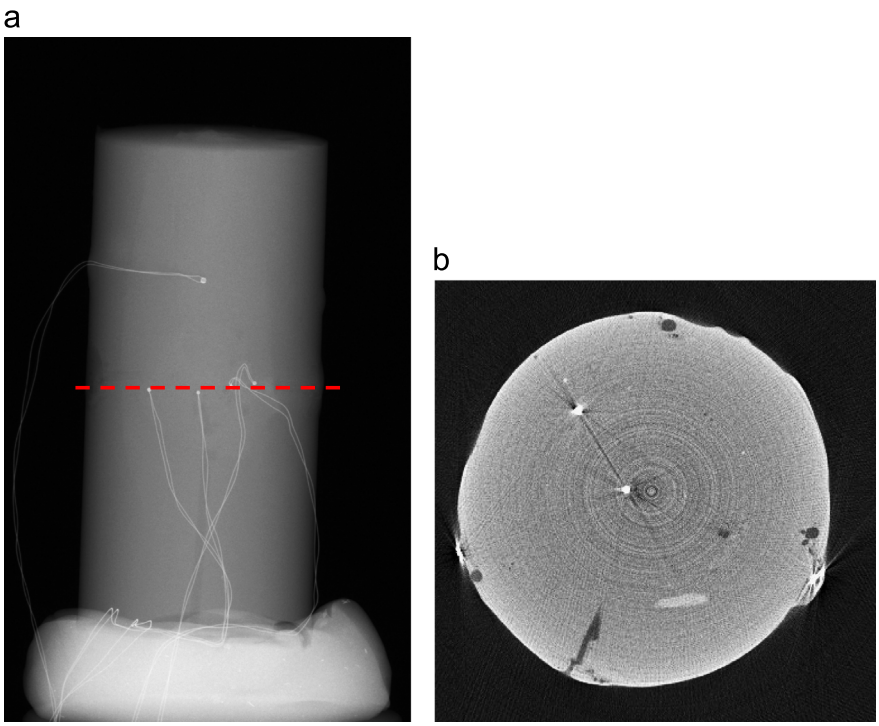


**Fig. 2.** (a) Grey scale radiogram of phantom B with thermocouples (white lines) (b) Tomographic grey scale image of the slice along the red line (dashed) in (a). The bright white points are the head of the thermocouples, the darker gray areas are air bubbles. (For interpretation of the references to color in this figure legend, the reader is referred to the web version of this article.)

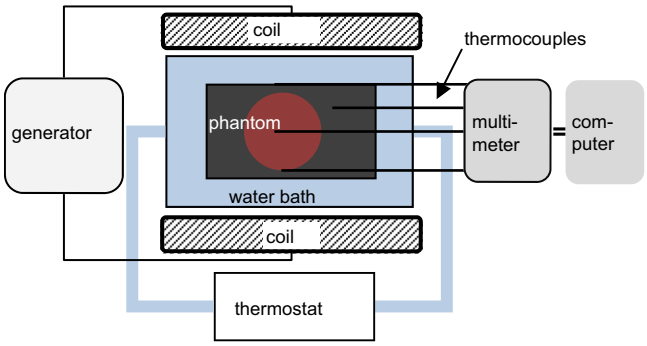


**Fig. 3.** Schematic representation of the experimental setup. (For interpretation of the references to color in this figure legend, the reader is referred to the web version of this article.)

15 mm although the real spheres also differ slightly in shape and diameter. However, the central point of each sphere has been exactly detected and implemented into the simulation model.

Additionally to the geometrical shape, material parameters are summarized in Table 4. The density of PUR was set to 1546 kg/m³ [33] and heat conductivity was proved out experimentally. Therefore, a defined mass of PUR was heated up to a defined temperature; afterwards it has been placed in a known amount of cold water inside of a Dewar vessel. The temperature change has been detected with a thermocouple. Since the heat capacity of water is well known, the heat capacity of PUR could be calculated.

## 3. Experimental results

### 3.1. Phantoms A, B, C

As expected, the temperature increased in all three phantoms with increasing magnetic field strength. In Fig. 5 the temperature profile of phantom B is shown. The highest temperature difference was measured (black-rectangle) in the center of the enriched sphere. A minor temperature increase has been detected at the border regions of the phantom.

To the border of the phantoms a lower increase of the temperature was measured. The temperature is not only depending on the distance to the enriched sphere, but also on the distance to the surface of the phantom and therefore to the water bath. With more or less the same distance to the center of the sphere enriched with magnetic nanoparticle, the temperature difference measured with the red (▲) thermocouple, with is around 1 mm from the cooling water bath, is 0.1 K less than measured with the green (▼) thermocouple, having a distance to the water bath of around 8 mm.

### 3.2. Phantom D

Also in phantom D the temperature increases with increasing magnetic field strength. The highest temperature was measured in the center of the spheres. The difference between the temperatures of spheres 1 and 2 can be explained by the different distance of the thermocouple to the center of each sphere.

In Fig. 6 the temperature profile of phantom B is shown. In the center of the enriched sphere the highest temperature difference was measured (black-rectangle). Towards the border regions of the phantom the rise of temperature is less than in the middle of the phantom. As already found for phantoms A, B, and C the temperature depends on the distance to the enriched sphere as well as on the distance of the phantom's surface to the water bath.

## 4. Simulation results

In Fig. 7 the simulated temperature profile for a magnetic field strength of 8.7 kA/m is shown in (a) for phantom B and in (b) for phantom D. The hottest part is in the center of the ferrofluid enriched area and the temperature decreases towards the surface

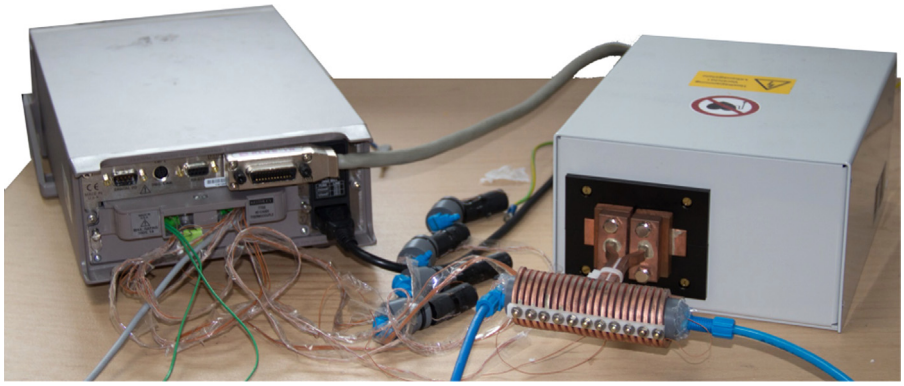

**Fig. 4.** Magnetic coil with the multimeter and all phantoms used. The phantoms were placed inside the water bath which is positioned in the coil.

**Table 3**
Heating capacities used in the simulation depending on the simulated magnetic field strength.

| Magnetic field strength [kA/m] | heating capacity [kW/m$^3$] |
|---|---|
| 4.4 | 15 |
| 5.3 | 20 |
| 6.2 | 25 |
| 7.0 | 30 |
| 7.9 | 35 |
| 8.7 | 40 |

**Table 4**
Material parameters used for the simulations.

| Volume/material | Parameter | | |
|---|---|---|---|
| Sphere | Heat conductivity | $\lambda$ | 0.65 W/m K |
| | Heat capacity | $c_p$ | 1400 J/kg K |
| | Density | $\rho$ | 1546 kg/m³ |
| Cylinder | Heat conductivity | $\lambda$ | 0.65 W/m K |
| | Heat capacity | $c_p$ | 1400 J/kg K |
| | Density | $\rho$ | 1546 kg/m³ |
| Water | Heat conductivity | $\lambda$ | 0.626 W/m K |
| | Heat capacity | $c_p$ | 4186 J/kg K |
| | density | $\rho$ | 993.3 kg/m³ |

of the phantom. Phantom D shows also the overlap of the temperature profile between the two spheres.

## 5. Comparison of measured and simulated results

To compare the measured and the simulated data, the temperatures at the exact positions of the thermocouples (measured by X-ray tomography) were plotted. In Fig. 8 the measured and simulated temperatures are depicted for different magnetic field strengths and for all phantoms.

The simulated data (lines) shows a good agreement with the measured data (symbols).

Only the temperature measured in the middle of phantom C (Fig. 8, bottom left, orange ▲) shows a larger deviation. This can be explained by the fact that the head of the thermocouple was incidentally positioned inside an air bubble which was included during the mixing of the phantoms' components. Because of the insulation effect of air the temperature measured in the air bubble is less than at the same position in full PUR. Furthermore, because of the air bubble less heating material is in the sphere of phantom C. This might also explain the difference between the experimental and simulated results. Except this thermocouple the

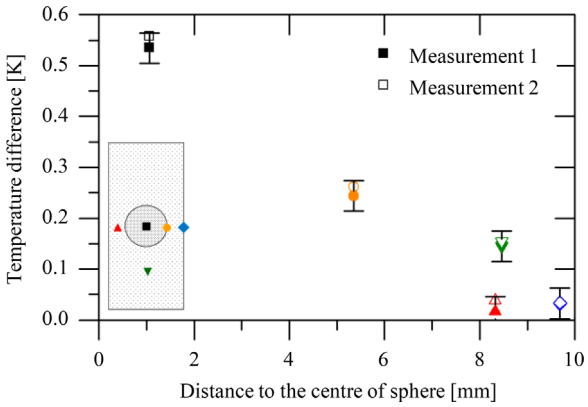


**Fig. 5.** Temperature (with reproduction) measured in Phantom B with a magnetic field strength of $H=8.7$ kA/m plotted over the distance to the centre of the sphere.

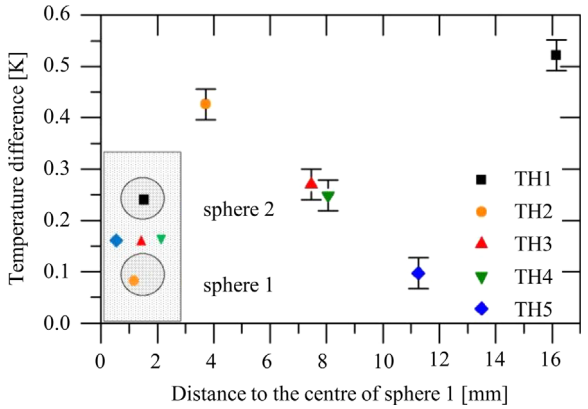


**Fig. 6.** Temperature measured in Phantom D with a magnetic field strength of $H=8.7$ kA/m plotted over the distance to the centre of sphere 1.

simulated show an agreement with the experimental data (see Fig. 8).

As a consequence, the experiments have shown an influence not only depending on the distance to the spheres enriched with magnetic particles, but also on the distance to the water bath. Thus, using the experimental results it is not possible to compare the temperature profile, since the thermocouples are on different positions inside the respective phantoms. However the simulated and the measured temperatures show an agreement, therefore it is possible to compare the simulated temperature profiles (see Fig. 9).

As can be seen (Fig. 9), the temperature in phantom C increases significantly (0.95 K) compared to the temperatures in phantom B

(0.55 K) and phantom A (0.15 K). This difference can be explained by the fact that the surface to volume ratio (shown in Table 2) is lower in phantom C than in phantom B and A.

Therefore in phantom A a higher heat loss occurs than in phantoms B and C. Consequently a higher magnetic field is necessary to achieve the same temperature difference.

## 6. Conclusion

The presented experimental study combines the experimental and simulative investigations of temperature profiles in four different phantoms to enable predictions of temperature profiles found during MHT.

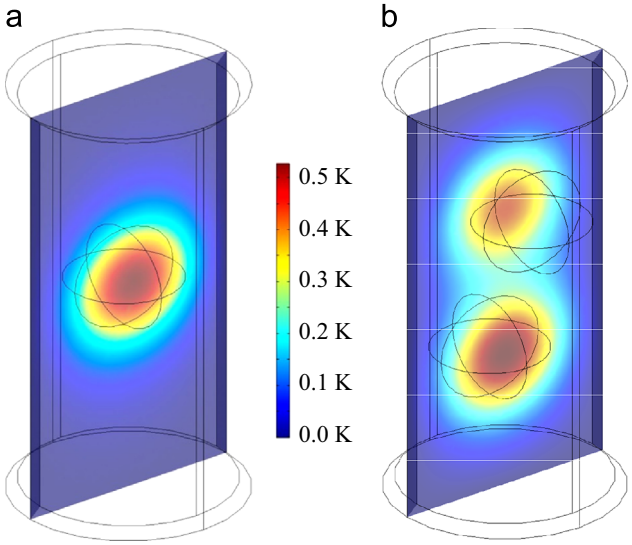


**Fig. 7.** Simulation results (a) of phantom B and (b) of the phantom D for a magnetic field strength of 8.7 kA/m.

During the experimental investigations the magnetic field strength was varied between 4.4 kA/m and 8.7 kA/m at a constant frequency of 284 kHz. Based on these results we established a simulation which shows an agreement with the measured temperature profiles.

It can be concluded that the maximum temperature depends on the volume-to-surface ratio. Nevertheless the strongest influence is created by the water bath and thus depends on the blood flow in biological tissue consequently. The results enable a further understanding of temperature distribution during MHT and should be taken into account for future investigations.

In summary, the experimental set up and conditions have been moved towards more realistic conditions and processes in biological tissue during MHT, but still benefit of simple geometries and comparatively easy behavior. In the result the prediction of heat transition behaviour is enabled, and thus to study and to be able to predict it from non-invasive temperature measurements of the outer tissue surface. Consequently, the possible impact on

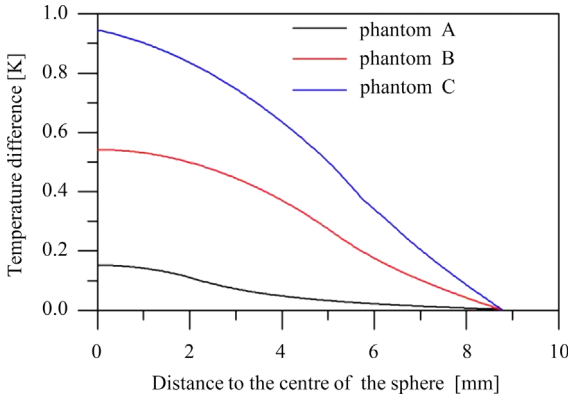


**Fig. 9.** Simulated temperature profiles in the phantoms A, B, C for a magnetic field strength of 8.7 kA/m.

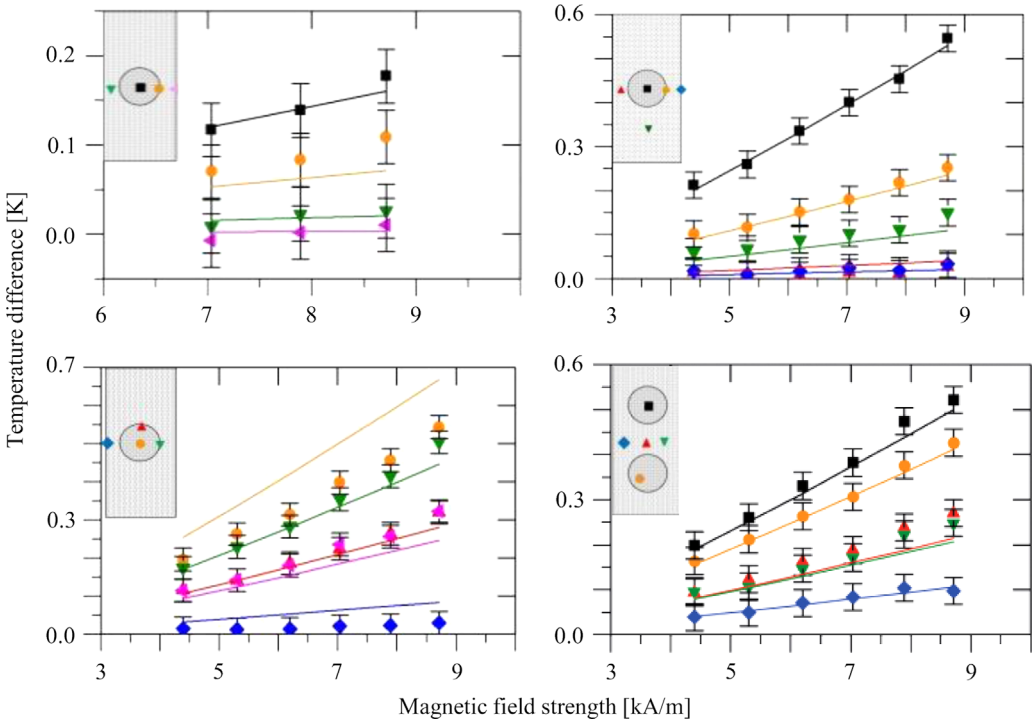


**Fig. 8.** Comparison of simulated temperature (lines) and measured data (symbols) of Phantom A (top left), B (top right), C (bottom left) and D (bottom right).

the theoretical use of MHT in therapy is a reduction of negative influence on the patients comfort.

## Acknowledgment

We thank Elantas Bectron for providing the polyurethane gel. This work has been financially supported by Deutsche Forschungsgemeinschaft (DFG) under Grant number Od18/13-3.

## References

[1] S. Dutz, J.H. Clement, D. Eberbeck, T. Gelbrich, R. Hergt, R. Müller, J. Wotschadlo, M. Zeisberger, Ferrofluids of magnetic multicore nanoparticles for biomedical applications, J. Magn. Magn. Mater. 321 (2009) 1501–1504.
[2] Q.A. Pankhurst, J. Connolly, S. Jones, J. Dobson, Applications of magnetic nanoparticles in biomedicine, J. Phys. D: Appl. Phys. 36 (2003) R167.
[3] Q. Pankhurst, N. Thanh, S. Jones, J. Dobson, Progress in applications of magnetic nanoparticles in biomedicine, J. Phys. D: Appl. Phys. 42 (2009) 224001.
[4] S. Odenbach, Colloidal Magnetic Fluids: Basics, Development and Application of Ferrofluids, Springer, 2009.
[5] A.S. Lübbe, C. Bergemann, J. Brock, D.G. McClure, Physiological aspects in magnetic drug-targeting, J. Magn. Magn. Mater. 194 (1999) 149–155.
[6] A.S. Lübbe, C. Bergemann, H. Riess, F. Schriever, P. Reichardt, K. Possinger, M. Matthias, B. Dörken, F. Herrmann, R. Gürtler, Clinical experiences with magnetic drug targeting: a phase I study with 4′-epidoxorubicin in 14 patients with advanced solid tumors, Cancer Res. 56 (1996) 4686–4693.
[7] R. Tietze, R. Jurgons, S. Lyer, E. Schreiber, F. Wiekhorst, D. Eberbeck, H. Richter, U. Steinhoff, L. Trahms, C. Alexiou, Quantification of drug-loaded magnetic nanoparticles in rabbit liver and tumor after in vivo administration, J. Magn. Magn. Mater. 321 (2009) 1465–1468.
[8] R. Tietze, S. Lyer, S. Dürr, T. Struffert, T. Engelhorn, M. Schwarz, E. Eckert, T. Göen, S. Vasylyev, W. Peukert, Efficient drug-delivery using magnetic nanoparticles—biodistribution and therapeutic effects in tumour bearing rabbits, Nanomed. Nanotechnol. Biol. Med. 9 (2013) 961–971.
[9] I. Hilger, R. Hergt, W.A. Kaiser, Towards breast cancer treatment by magnetic heating, J. Magn. Magn. Mater. 293 (2005) 314–319.
[10] I. Hilger, W. Andrä, R. Hergt, R. Hiergeist, H. Schubert, W.A. Kaiser, Electromagnetic heating of breast tumors in interventional radiology: in vitro and in vivo studies in human cadavers and mice 1, Radiology 218 (2001) 570–575.
[11] I. Hilger, A. Rapp, K.-O. Greulich, W.A. Kaiser, Assessment of DNA damage in target tumor cells after thermoablation in mice 1, Radiology 237 (2005) 500–506.
[12] H. Mamiya, B. Jeyadevan, Hyperthermic effects of dissipative structures of magnetic nanoparticles in large alternating magnetic fields, Sci. Rep. 1 (2011).
[13] A. Jordan, R. Scholz, P. Wust, H. Fähling, J. Krause, W. Wlodarczyk, B. Sander, T. Vogl, R. Felix, Effects of magnetic fluid hyperthermia (MFH) on C3H mammary carcinoma in vivo, Int. J. Hyperthermia 13 (1997) 587–605.
[14] A. Jordan, R. Scholz, P. Wust, H. Fähling, R. Felix, Magnetic fluid hyperthermia (MFH): cancer treatment with AC magnetic field induced excitation of biocompatible superparamagnetic nanoparticles, J. Magn. Magn. Mater. 201 (1999) 413–419.
[15] A. Jordan, R. Scholz, K. Maier-Hauff, M. Johannsen, P. Wust, J. Nadobny, H. Schirra, H. Schmidt, S. Deger, S. Loening, Presentation of a new magnetic field therapy system for the treatment of human solid tumors with magnetic fluid hyperthermia, J. Magn. Magn. Mater. 225 (2001) 118–126.
[16] M. Johannsen, B. Thiesen, P. Wust, A. Jordan, Magnetic nanoparticle hyperthermia for prostate cancer, Int. J. Hyperthermia 26 (2010) 790–795.
[17] S. Laurent, S. Dutz, U.O. Häfeli, M. Mahmoudi, Magnetic fluid hyperthermia: focus on superparamagnetic iron oxide nanoparticles, Adv. Colloid Interface Sci. 166 (2011) 8–23.
[18] K. Maier-Hauff, R. Rothe, R. Scholz, U. Gneveckow, P. Wust, B. Thiesen, A. Feussner, A. von Deimling, N. Waldoefner, R. Felix, Intracranial thermotherapy using magnetic nanoparticles combined with external beam radiotherapy: results of a feasibility study on patients with glioblastoma multiforme, J. Neuro-oncol. 81 (2007) 53–60.
[19] M. Krukemeyer, W. Wagner, M. Jakobs, V. Krenn, Tumor regression by means of magnetic drug targeting, Nanomedicine 4 (2009) 875–882.
[20] K. Gitter, S. Odenbach, Experimental investigations on a branched tube model in magnetic drug targeting, J. Magn. Magn. Mater. 323 (2011) 1413–1416.
[21] K. Gitter, S. Odenbach, Quantitative targeting maps based on experimental investigations for a branched tube model in magnetic drug targeting, J. Magn. Magn. Mater. 323 (2011) 3038–3042.
[22] R. Tietze, H. Rahn, S. Lyer, E. Schreiber, J. Mann, S. Odenbach, C. Alexiou, Visualization of superparamagnetic nanoparticles in vascular tissue using XμCT and histology, Histochem. Cell Biol. 135 (2011) 153–158.
[23] R. Gilchrist, R. Medal, W.D. Shorey, R.C. Hanselman, J.C. Parrott, C.B. Taylor, Selective inductive heating of lymph nodes, Ann. Surg. 146 (1957) 596.
[24] W. Andrä, C. d'Ambly, R. Hergt, I. Hilger, W. Kaiser, Temperature distribution as function of time around a small spherical heat source of local magnetic hyperthermia, J. Magn. Magn. Mater. 194 (1999) 197–203.
[25] O. Arndt, J. Strutz, W. Mann, Praxis der HNO-Heilkunde, Kopf-und Halschirurgie: 265 Tabellen, Georg Thieme Verlag, 2010.
[26] F. Henrich, H. Rahn, S. Odenbach, Investigation of heat distribution during magnetic heating treatment using a polyurethane–ferrofluid phantom-model, J. Magn. Magn. Mater. 351 (2014) 1–7.
[27] H. Rahn, S. Schenk, H. Engler, S. Odenbach, Tissue model for the study of heat transition during magnetic heating treatment, IEEE Trans. Magn. 49 (2013) 244–249.
[28] Omega, in, ⟨http://www.omega.com⟩, 2014.
[29] Lakeshore, in, ⟨http://www.lakeshore.com⟩, 2014.
[30] D. Günther, D.Y. Borin, S. Günther, S. Odenbach, X-ray micro-tomographic characterization of field-structured magnetorheological elastomers, Smart Mater. Struct. 21 (2012) 015005.
[31] T. Borbáth, S. Günther, D.Y. Borin, T. Gundermann, S. Odenbach, XμCT analysis of magnetic field-induced phase transitions in magnetorheological elastomers, Smart Mater. Struct. 21 (2012) 105018.
[32] H. Hensel, K.D. Bock, Durchblutung und Wärmeleitfähigkeit des menschlichen Muskels, Pflugers Arch. Eur. J. Physiol. 260 (1955) 361–367.
[33] Elantas, in, ⟨http://www.elantas.com⟩, 2014.
[34] Ferrotec, in, ⟨http://www.ferrotec.com⟩ 2014.
[35] J. Nowak, D. Wolf, S. Odenbach, A rheological and microscopical characterization of biocompatible ferrofluids, J. Magn. Magn. Mater. 354 (2014) 98–104.
[36] S. Dutz, Nanopartikel in der Medizin: magnetische Eisenoxid-Nanopartikel für intrakorporale Erwärmungsanwendungen, Kovač (2008).
[37] Comsol, 2014, in, ⟨http://www.comsol.com/⟩.